Fading due to static and dynamic features in a factory environment on wireless channels

Alexandra E Curtin, David R Novotny, Richard Candell, Galen Koepke, Peter Papazian, Jeanne Quimby, and Kate Remley

National Institute of Standards and Technology, Boulder, CO

Abstract*—Channel sounding of dense or complex environments, such as industrial or factory spaces, is an important consideration when increasing the deployment of current and next-generation wireless technologies. The deployment of machine–to-machine or vehicle-to-vehicle communications is of particular interest in the factory space as the dense environment provides a challenging test case. Here, we present results from a mobile channel sounder operating near the ISM (industrial, scientific, and medical) radio bands at 2.245 GHz and 5.400 GHz within a large factory space. We consider the possibility of both fast and slow fading effects due to our mobile receiver cart and due to other moving equipment in the space. Of critical importance to the validity of these measurements is the synchronization of the tether-less channel sounder using rubidium (Rb) clocks. The root mean squared (RMS) delay spread, Doppler spread, and fading results are presented for various experimental configurations, including different transmitter antenna locations, straight-line receiver cart paths, and stationary measurements collected in the presence of moving equipment.

I. Introduction

Channel sounding is important for the rapid improvement and introduction of new wireless communications technology in factory environments. Knowledge of a channel provides a baseline for quantifying communications capacity and performance. There is increasing desire to deploy wireless mobile-to-mobile infrastructure in factory environments that are densely populated with both stationary and moving machinery. Additionally, some factory operations will involve adopting wireless solutions for equipment control. To ensure proper tool function and human safety, such applications of wireless technology must function with high reliability in an environment containing a variety of non-line-of-sight (NLOS) and fading conditions.

This measurement effort was aimed at quantifying wireless channels in dense and dynamic factory environments. In this effort, we characterized two government channels adjacent to commonly-used ISM (industrial, scientific, and medical) bands at 2.45 GHz and 5.80 GHz. We performed measurements in a machine shop at the National Institute of Standards and Technology, Gaithersburg, MD Laboratories, at an automotive plant in Detroit, MI, and at a steam plant at the National Institute of Standards and Technology, Boulder, CO Laboratories. The analysis presented here will focus on the measurements collected at the much larger space in Detroit, considering both the effects of moving the receiver cart along a set of walkways and of parking the cart in a dense area near moving equipment. The data from these measurement campaigns is available at http://doi.org/10.18434/T4453N. The plant floor was not only populated with large stationary apparatus, but also had a wide variety of moving metal bodies including gantry systems, automotive robots, electric vehicles, and self-guided vehicles. For both measurement configurations, we look at the RMS delay spread, and at Doppler and fading effects due to cart and environmental motion.

II. Instrumentation

The photo in Figure 1 shows the transmitter and receiver units of this real-time, correlation-based channel sounder. Each side has a National Instruments PXI chassis containing our timing and synchronization modules, vector signal transceivers (VST), and control software.[1] The VSTs are set up to generate and receive pseudo-random noise (PN) codes at 2.245 GHz and 5.400 GHz. In order to look at the channel and different fading behaviors in our measured environment at each of these frequencies, we need precise timing information. For the purposes of this paper, the relevant details of the instrumentation have to do with the timing and synchronization modules and the Rb clocks they are connected to.

To quantify all the losses in our system, we performed a back-to-back calibration of the equipment by connecting the line for the transmit antenna through a 50-dB attenuator to the filtered amplifier on the receiver cart [1]. By varying input power we were able to do a linearity check each time we switched frequencies. The receiver chassis collected I/Q (in-phase, quadrature) data for this back-to-back test, recording a reference signal to use in normalizing the losses and delay in all of our subsequently collected data. The strength of the back-to-back method of calibration is that it gives us a relative insertion loss without power measurements.

Figure 2 shows a block diagram of the entire setup, including the three connections from each of the Rb clocks to the two chasses. Each PXI chassis receives multiple signals from its own associated Rb clock. The clocks were disciplined to each other by a direct connection between them for 24-48 hours before being connected for testing. Each chassis received a 1 pulse-per-second (PPS) signal and two 10-MHz signals from its clock. The 1 PPS signal was sent into the 6683H timing card at the PFI0 input to trigger the PN codeword pulse every

[1]Certain trade names and company products are mentioned in the text. In no case does such identification imply endorsement of these products and equipment by the National Institute of Standards and Technology, nor does it imply that the products are necessarily the best available for the purpose.

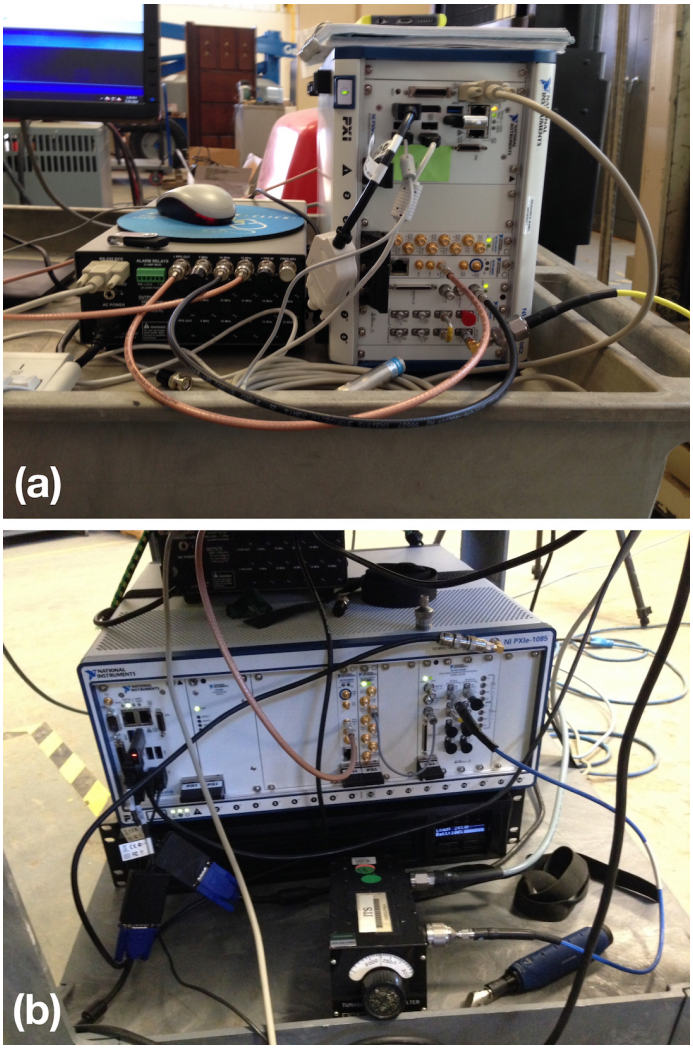

Fig. 1: Photos of the (a) transmitter and (b) receiver setups. The amplifier, filter, and antennas are not shown. The details of the connections in these photos, and the complete setup, are depicted in Figure 2.

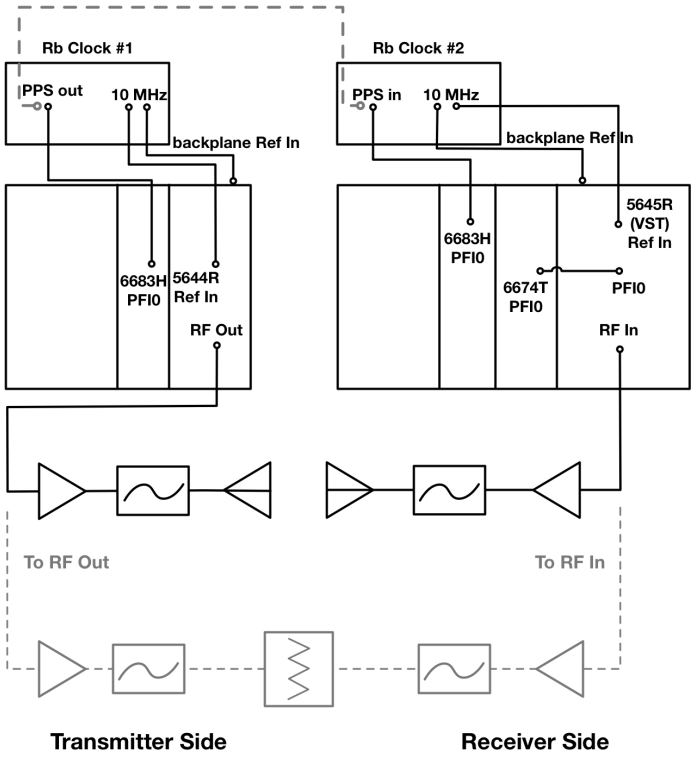

Fig. 2: A block diagram of the transmitter and receiver setups. The left side represents the stationary transmitter cart and equipment, and the right side represents the mobile receiver cart and equipment. In each case the 10 MHz clock signals are routed into the National Instruments chassis. The grey dashed lines show the connections present when synchronizing the chassis, and when determining the losses in the system. The top grey line shows the PPS signals between the clocks connected, as is required for 24-48 hours to get sub-nanosecond accuracy. The lower part of the schematic shows connecting the two chassis through a 50-dB attenuator in order to measure a back-to-back reference signal.

N code words on the transmit chassis and to trigger the listen on the same card on the receive chassis. Each chassis received a 10-MHz signal to govern the backplane clocks. The second 10-MHz signal went into the 5646R VST card on the receive chassis and the 5644R VST card reference training signal on the transmit chassis to ensure up-conversion coherence. It is this last 10-MHz signal that was instrumental in setting the time reference and disciplining the chassis clocks after syncing, providing down- and up-conversion coherency and removing the phase ambiguity caused by relying on the chassis clocks integrated into the backplane. The primary drift factor is the drift between the Rb clocks once disconnected, at an average rate of <8 ns over a 4-hour data acquisition run. Initially, jostling the cart during the runs cause larger deviations in synchronization, leading us to cushion the mounting of the receiver chassis to its mobile cart in later measurements.

The channel sounder as configured is capable of covering the spectrum from 65 MHz to 6 GHz at 200-MHz bandwidth [2]. For these measurements, the signal from the transmit chassis was passed through an amplifier (model varied based on frequency) and bandpass filter to give us roughly 1.25 W transmit power at 2.245 GHz and 1.7-2 W transmit power at 5.400 GHz. The power was selected to be within the range where output power from the amplifier was linear in input power, as well as within the level allowed by our transmit authorization. The received signal is collected as complex I and Q waveform data. The timing of triggers, oversampling, delays between codewords and division of data into arrays and files are all configurable. Received data were referenced against a back-to-back calibration:

$$1 \text{ codeword} = 2047 \text{ symbols} \quad (1)$$

$$1 \text{ record} = 8188 * 12.5\ ns = 102\ \mu s \quad (2)$$

$$\text{trigger} = 200 * (102\ \mu s) = 20.47\ ms \quad (3)$$

$$\text{acquisiton} \cong 6 \text{ seconds of data} \quad (4)$$

Each data record represented the transmission of a single PN codeword, with 12.5-ns symbol time and 4x oversampling. A single record was 102 μs long. The receiver software was configured to acquire data every 200 codewords, or roughly every 20 ms. In order to save data to disk, we chronologically

binned groups of records together in "acquisitions" saving 300 records into an acquisition, and 20 acquisitions into a file.

This method of collecting the data with a 20-ms trigger time and with binning into acquisitions determined (1) the range of velocities we could detect and (2) the length of time over which we maintained phase coherency. Each time our control software incremented to the next acquisition we lost uniform sampling while there was a gap in the data. This meant we had phase coherency in 6-s time blocks. We improved our time or spatial resolution of velocity calculations by looking at smaller blocks of records; e.g., 100 records or 2 seconds of data, within an acquisition. The range of velocities we could detect was fixed by the trigger interval and the wavelength of the signal such that at 2.245 GHz:

$$v_{max} = \frac{wavelength}{sample\ time} \tag{5}$$

$$= \frac{0.1335\ m}{20.47\ ms} = 6.52\frac{m}{s} \tag{6}$$

$$v_{range} = \pm\frac{1}{2}V_{max} \tag{7}$$

$$= \pm\ 3.206\ m/s \tag{8}$$

The method for calculating velocity at all points along paths walked in the factory space is left to the discussion section of this paper, Section 3.4.

III. Results and Discussion

Data were collected for several different patterns of movement through the measurement environments. Measurements were taken in two modes, first while walking a continuous path through the factory floor and second by walking a smaller path through a dense array of automated moving equipment, with 2-minute pauses at three regions of interest. This second set of measurements was particularly well-tailored to the automotive-plant environment where we hoped to observe the effect of a metal "canyon" of large mills and gantry crane systems moving while the receiver antenna was stationary.

The recorded I/Q data were processed in a variety of ways to look at impulse response, power delay, and fading behavior. We looked at the fading behavior observed both when the receiver antenna was stationary with equipment moving past it and when the cart was traveling at a constant speed in different parts of the measurement environment.

A. Impulse Responses

The first analysis of our data was to calculate power delay profiles (PDPs), as defined in terms of the channel impulse response (CIR), with the goal of studying how these change with time. We have considered two methods to filter the data. Filtering the data limits Gibbs ringing and improves the presentation and signal-to-noise ratio of the data. The two simplest methods are (1) to filter the CIR with the original PN code and (2) to transform the CIR into the frequency domain and truncate the response before the first nulls. The sampling time determines the 80-MHz bandwidth for our instrument, with the first nulls occurring at $\pm$ 20 MHz.

In all cases, the unfiltered CIR is defined as: [1] [3]

$$CIR\,(t) = \mathfrak{F}^{-1}\left(\frac{\mathfrak{F}(meas)}{\mathfrak{F}(ref)}\right) * 10^{\frac{-atten}{20}} \tag{9}$$

$$PDP\,(t) = 10 * log_{10}|CIR|^2 \tag{10}$$

Here $\mathfrak{F}(meas)$ and $\mathfrak{F}(ref)$ represent the Fourier transforms of the time-domain IQ data from the measured run and from the most recent back-to-back calibration, respectively. By putting $\mathfrak{F}(ref)$ in the denominator, we output a calibrated PDP. The attenuator is inserted at the end to offset the -50 dB attenuator used in the back-to-back calibration that is used for the reference signal. We can inverse the Fourier transform back to the time domain to look at the change in PDP with varying distance between the transmitter and receiver chassis.

Filtering this CIR with the transmitted PN code is a typical means of further lowering the noise floor. For our analysis, the PN filter, $w(f)$, and the filtered CIR are given as [2]:

$$w\,(f) = \frac{\mathfrak{F}\,(PN) \times \mathfrak{F}\,(PN^*)}{\sqrt{\sum |PN|^2}} \tag{11}$$

$$CIR_{filt}\,(t) = \mathfrak{F}^{-1}\left(\frac{\mathfrak{F}(meas)}{\mathfrak{F}(ref)} * w(f)\right) * 10^{\frac{-atten}{20}} \tag{12}$$

For a PN code consisting of rectangular symbols in the time domain, we expect the filter to look like a sinc function in the frequency domain. Scaled to have an amplitude of one, this filter produces a broadening of our unfiltered PDP and lowers the peak power [2]. At 2.245 GHz, the scaling factor in the denominator of (11) produces a 6.3-dB offset that raises the filtered peak enough to equate the power under the curve to the unfiltered curve.

The alternate method of bandwidth filtering relies on calculating the CIR in the frequency domain [equation (9) without the inverse Fourier transform]. To filter within the first null, we truncate the frequency response at $\pm$ 90 $\%$ of the first null, or the central 36 MHz. We will discuss this method of filtering later as a means of looking for high velocity contributions to our signal.

If we analyze the PDPs collected while traveling through different sections of the factory space, we can look at the changes in fading and delay spread due to performing known movements. Observable changes may also occur due to the environment while the cart is stationary in the metal canyon (e.g., changes in arrival time due to motion of gantry cranes and other large equipment).

B. Delay Spread

At 2.245 GHz and at 5.400 GHz, we analyzed two segments of data collected in the automotive transmission assembly plant. These segments are part of two longer paths shown in Figure 3 that looped through the factory space, passing by machining and storage locations. The receiver cart was manually pushed, and some inconsistencies may be expected. Turns, line-of-sight, and other factors mean that the cart may slow down (as in turns) or that moving equipment or the

direction of travel may cause other Doppler contributions to occur.

The first dataset was collected while holding our receiver stationary in a metal canyon at waypoint I3.1 in Figure 3(b). The second dataset was collected while rolling our receiver cart along a wide aisle from the transmitting antenna to the first corner at waypoint 2 in Figure 3(a). The stationary dataset covered roughly one minute of collection time. From the average delay time and rms delay spread, we are able to gain both quantitative and qualitative information about the wireless environment.

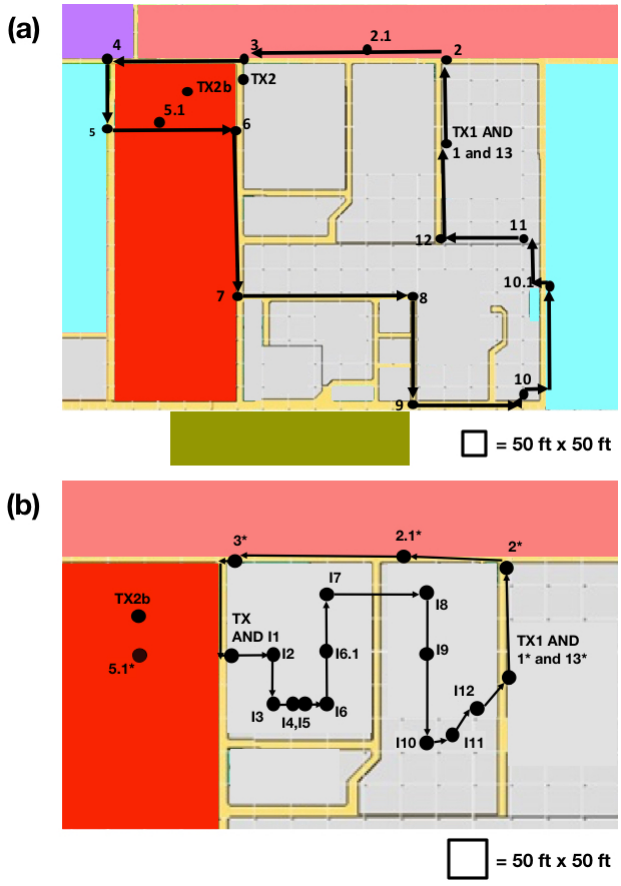

Fig. 3: (a) A map of the "outer" path taken by the receiver cart within the factory space. Colored blocks represent work areas of varying purposes. Walkways and self-guided vehicle paths separate these areas. Each numbered dot represents a waypoint where the acquisition number was noted in real time. Transmit antenna locations are "TX". (b) The "short" or "inner" path. Waypoints unique to this path are labeled with an "I", and waypoints common to both inner and outer paths receive an "*". At locations I3 and I6.1, the cart paused for two 2-minute intervals to measure in a metal canyon where equipment was moving past the receive antenna.

The average delay time may be calculated as [4], [5]:

$$T_D = \frac{\int_0^{\tau_e} \tau p(\tau)\, d\tau}{\int_0^{\tau_e} p(\tau)\, d\tau}, \tag{13}$$

where τ is defined to be $t - t_a$, the sample time minus the time of the first arrival peak and τ_a is the arrival time of the first peak [5], [6]. The limit τ_e is the time of the last data sample, sometimes defined as the last data sample above the cutoff threshold. In our case, we have 8188 discrete samples, so τ_e and τ_a are equal to 8188, and the first arrival sample number times $\Delta t = 12.5$ ns, respectively. The discrete nature of the data means we can usefully express T_D as a sum. Additionally, since we compute our impulse responses by normalizing against the back-to-back reference measurement, there is no need to divide by total power. In using the impulse response for $p(\tau)$, however, we need to implement proper thresholds. Although filtering with the PN filter as noted in Equation (11) and (12) lowers the noise floor, the CIRs used to calculate average time delay and rms delay spread include an additional step. The noise floor was calculated and a threshold was applied to only include CIR data more than 10 dB above the noise floor and within 30dB of the primary peak. [4]. The equation for calculating average time delay from this cleaner CIR is then:

$$T_D = \sum_{n=1}^{8188} n\Delta t |CIR(n)|^2. \tag{14}$$

From the average time delay, we can also calculate the RMS delay spread:

$$S = \sqrt{\frac{\int_0^{\tau_e} (\tau - T_D)^2\, p(\tau)\, d\tau}{\int_0^{\tau_e} p(\tau)\, d\tau}}, \tag{15}$$

which in a discrete case with a normalized CIR becomes: [5]

$$S = \sqrt{\sum_{n=1}^{8188} (n\Delta t - T_D)^2\, |CIR(n)|}. \tag{16}$$

Over the one-minute block of stationary data collection at 2.245 GHz, we acquired 3000 records of I/Q data. The first peak had a mean arrival time of 167 ns. The standard deviation in the first arrival time was less than two samples. The average time was 391.3 ns and the RMS delay spread was 111.9 ns, as initially calcualted by [4]. The same analysis applied to stationary data collected at 5.400 GHz in a similar location showed a time of arrival of 254 ns. After inspecting the distances between the transmit antenna and these two collection locations, as well as the expected delay for the two signals at difference frequencies, we note that this 89 ns difference indicates a timing error or drift between the reference data and the collection. This drift of 7-8 samples cannot be accounted for by path differences between the datasets. The 5.400 GHz data had a mean time delay of 542.5 ns and a mean RMS delay spread of 154.6 ns [4]. Since the time of first arrival is factored out of the average delay calculation and RMS delay spread, these values are unaffected by the clock drift between the 5.400 GHz reference and this dataset.

Of particular interest is the behavior of the rms delay spread while the receiver cart was stationary at waypoint I3 and later as we moved from location 3* to location I1. In Figure 4(a) we show the rms delay spread for an entire short run. The plots are all cropped in time as there were no multiply-populated bins at higher delay times, just outliers. Figure 4(b) shows the delay spread for a 1-minute segment of the dwell time at location 3. The median delay time here is 119.7 ns, with an estimated full-width-half-maximum (FWHM) around 30 ns. Figure 4(c)

shows data from the same path, but this time traversing from waypoint 3* to I1. This segment is in an open area in front of the metal canyon, relative to the transmitting antenna. We have a line-of-sight here that is not present at waypoint I3, and we are moving perpendicular to the line from the transmitter to the metal canyon. The median delay time for this central peak is 85.9 ns, with an approximate FWHM of 60 ns. The setting in which the data were collected and the shape of the curves is noticeably different. The density of the equipment at waypoint I3 made for poor line-of-sight conditions. In contrast, the data shown in Figure 4(c) was collected in a much more open area, suggesting greater multi-path variation was allowed.

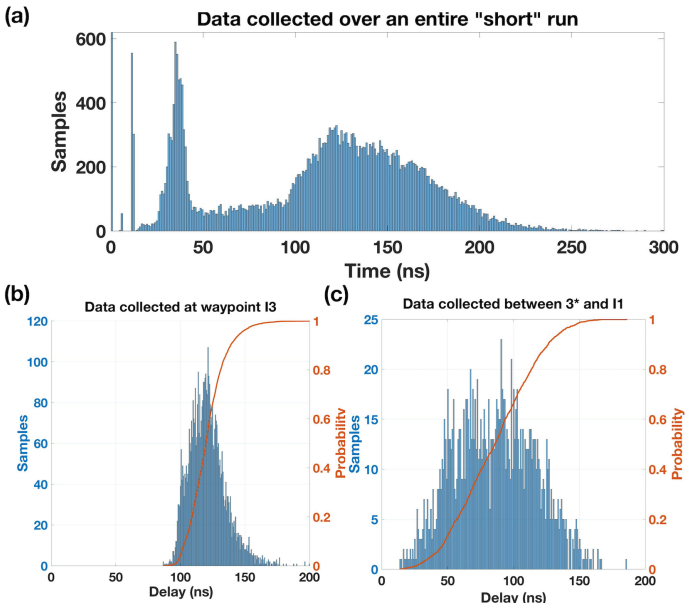

Fig. 4: Panel (a) shows the rms delay spread distribution for the entire run shown in 3b. Panels (b) and (c) separate the rms delay spread for the metal canyon at waypoint I3 and the segment from waypoint 3* to I1 in the same short run respectively.

Figure 5 shows the frequency response (a) and PDP (b) from one of our mobile data records collected at 5.400 GHz. In contrast to the stationary data, the mobile data clearly show the effect of the change in distance between the transmit and receive antennas as the receiver cart moves in a straight path away from the transmitter. Figure 5(c) shows the increasing time of arrival as the cart moves away from the transmitter antenna for the 5.400 GHz data.

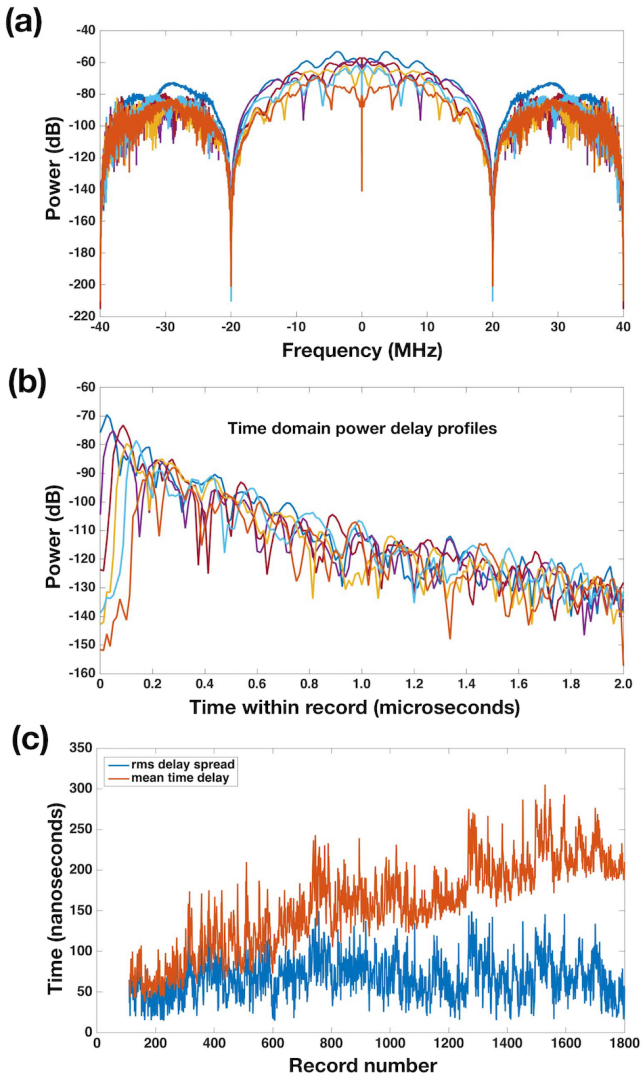

Fig. 5: Data plotted from the 5.400 GHz data moving the receiver cart from the tranmitter location TX1 to turn 2 in the long path. (a) Six frequency CIRs spanning 36 seconds of data. (b) PDPs from the same six records. (c) The rms delay spread and accompanying mean time delay for data collected between turns 1 and 2. The mean delay increases as expected as the receiver cart traverses the straight path from TX1 to the first turn. The rms delay spread remains relatively flat becoming slightly more noisy away from the TX location.

C. Path Loss

As noted previously, the dense nature of the factory environment means that the received signal is affected by more than the distance between the transmit and receive antennas. The path loss for an entire path through the factory space is calculated by taking the sum of the signal over only the time interval where the response is above the noise threshold. We set the threshold 30 dB below the maximum peak and take the sum over this interval from t_0 to $t_{threshold}$:

$$p\left(t\right) = \sum_{t=0}^{t_{threshold}} |CIR^2\left(t\right)|. \tag{17}$$

Figure 6 shows the path loss for the two long paths collected at 2.245 GHz and 5.400 GHz. Plotting the path loss versus time, we can match the path loss to waypoints in our path. Plotting the path loss versus the distance from each waypoint, we see that the path loss correlated not just to distance but also to the sharp reduction in signal quality as line-of-sight becomes obstructed.

D. Fading and Velocity

To consider Doppler effects and fading, we looked at the frequency, the bandwidth and sampling, and the cart velocity.

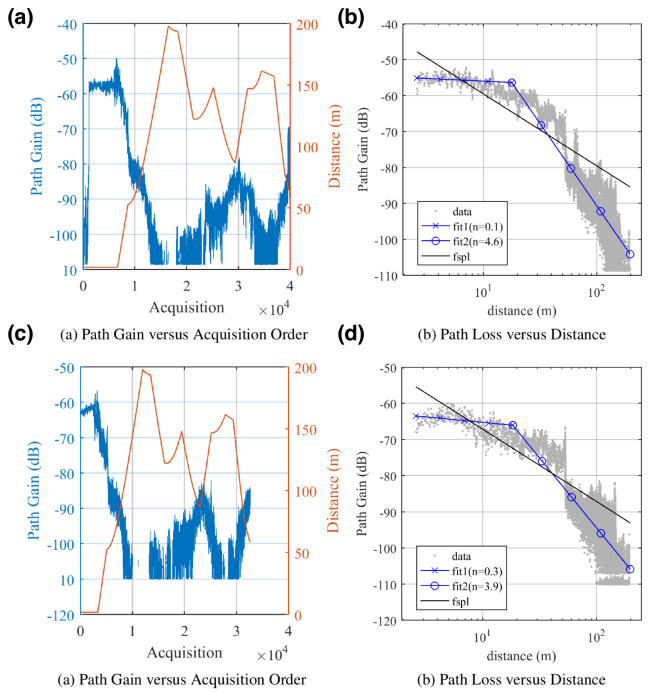

Fig. 6: Path loss calculated for (a) the outer path at 2.245 GHz and (c) at 5.400 GHz vs acquisition number (time). Path loss for the same data at both frequencies plotted vs distance from the transmitter in (b) and (d) respectively. Results provided by [4].

In order to see fast fading, we needed to collect data in a mode where the sample time T_s, or symbol duration, is longer than the coherence time, T_C of the channel. Slow fading is visible when the opposite is true. The coherence times of our 2.245 GHz and 5.400 GHz signals with the cart moving at approximately 1 m/s are 56 ms and 23.5 ms respectively, putting us in the regime where $T_C \gg T_s$. Each record is completed, as noted earlier, in 102 μs. The 200-codeword spacing means that triggering spaces these records 20.47 ms apart. Outside the research environment, the long coherence time would mean that our signals are only negligibly affected by Doppler fading in our environment.

We binned the acquired data into 100-record arrays of impulse responses $CIR(k,t)$, where k is the record number (or time location) in the array and t is the sample time within a record. When the data were collected, records were grouped into 300-record acquisitions and saved to disk every 20 acquisitions. In this mode, a single acquisition represented 6 seconds of data. Buffering between each acquisition to log data meant we did not have precise timing or phase information from one acquisition to the next. Our acquisitions are located in space by manual recording of acquisition and turn numbers. We easily stay within in an acquisition for calculating Doppler effects. The velocities of moving bodies and of the receiver cart extracted are completely dependent on Doppler shifts. The 100-record binning gives us roughly 2-s time and position resolution.

The time between records, 20.47 ms, defines the maximum Doppler shift we can measure to be 48.85 Hz, or a range of $\pm$ 24.43 Hz for objects moving away from or towards our transmit antenna. The 100-record binning means that the smallest Doppler shift we measure is 0.2047 or 0.4885 ms. For the 2.245-GHz data, this Doppler shift range defines the Doppler spectrum. The Doppler spectrum is calcuated as the Fourier transform of an array of CIRs in discrete symbol time bin, as discussed in [7]. Doppler shift in our data may be due not only to the motion of the cart at a supposed 1 m/s, but also to the motion of other objects in the factory environment. The velocity of the cart and these other bodies is proportionally related to the Doppler shift such that $\Delta v = \lambda \Delta f$, and the maximum velocity of objects we can resolve is $\lambda/20.47$ ms. For data collected at 2.245 GHz, the maximum velocity that we can observe is 6.52 m/s, or a range of $\pm$ 3.26 m/s. For the remainder of this work we discuss the observed Doppler behavior in terms of observed Doppler shifts and corresponding velocity of moving objects (including the receiver) relative to the transmit antenna.

Similar to calculating the Doppler power spectrum, the velocity distribution over a path can then be found by inverse Fourier transforming along the record number k direction such that each curve, $v_t(k)$ represents the velocity distribution of the signal at a particular sampling time t across all records:

$$v_t(k) = \mathfrak{F}^{-1}\left(CIR\left(k,t\right)\right) \tag{18}$$

$$v_t(k) = \frac{1}{N}\sum_{k=1}^{N} CIR(k,t) * e^{-2\pi \imath kt/N}. \tag{19}$$

Equation 19 defines the discrete inverse Fourier transform explicitly to further clarify the relationship between t and k for our three-dimensional data array (sample time, record number, power).

The outer path, Figure 3(a), was 148 acqusitions long, or 444 2-s time bins of 100 records. Performing this inverse Fourier transform 444 times, and selecting the time slice t containing the maximum amplitude in power when plotted as $v_t(k)$ vs power. Plotting these curves vs. time within the path produced the plot shown in Figure 7(a). Tying the time in the path to the waypoint marked in Figure 3(a), we can calculate velocity distribution and Doppler spectrum variation with time and receiver cart position.

The beginning of the data in Figure 7(a) shows a 0-velocity peak collected before the receiver cart began to move. Strong 1-m/s peaks then appear as the cart travels steadily away from the transmitter, and then reappear at the end of the path at -1 m/s as the cart returns. The 1-m/s cart speed correlated to a Doppler shift of roughly -7.5 Hz. In between, the dominant peaks still appear around 1 m/s, but line-of-sight, as determined by the placement of large storage and equipment blocks, plays a strong role in signal quality. After rounding the corner at waypoint 2, the noise level of the signal drops with overall level as the auto-gain routine attempts to adjust the signal level. Lower-velocity contributions may be attributed to turns.

Figure 7(b) shows power delay profiles collected while the receiver cart was traveling from waypoint 1 to 2 along the path in Figure 3(a). Figure 7(c) shows the corresponding Doppler

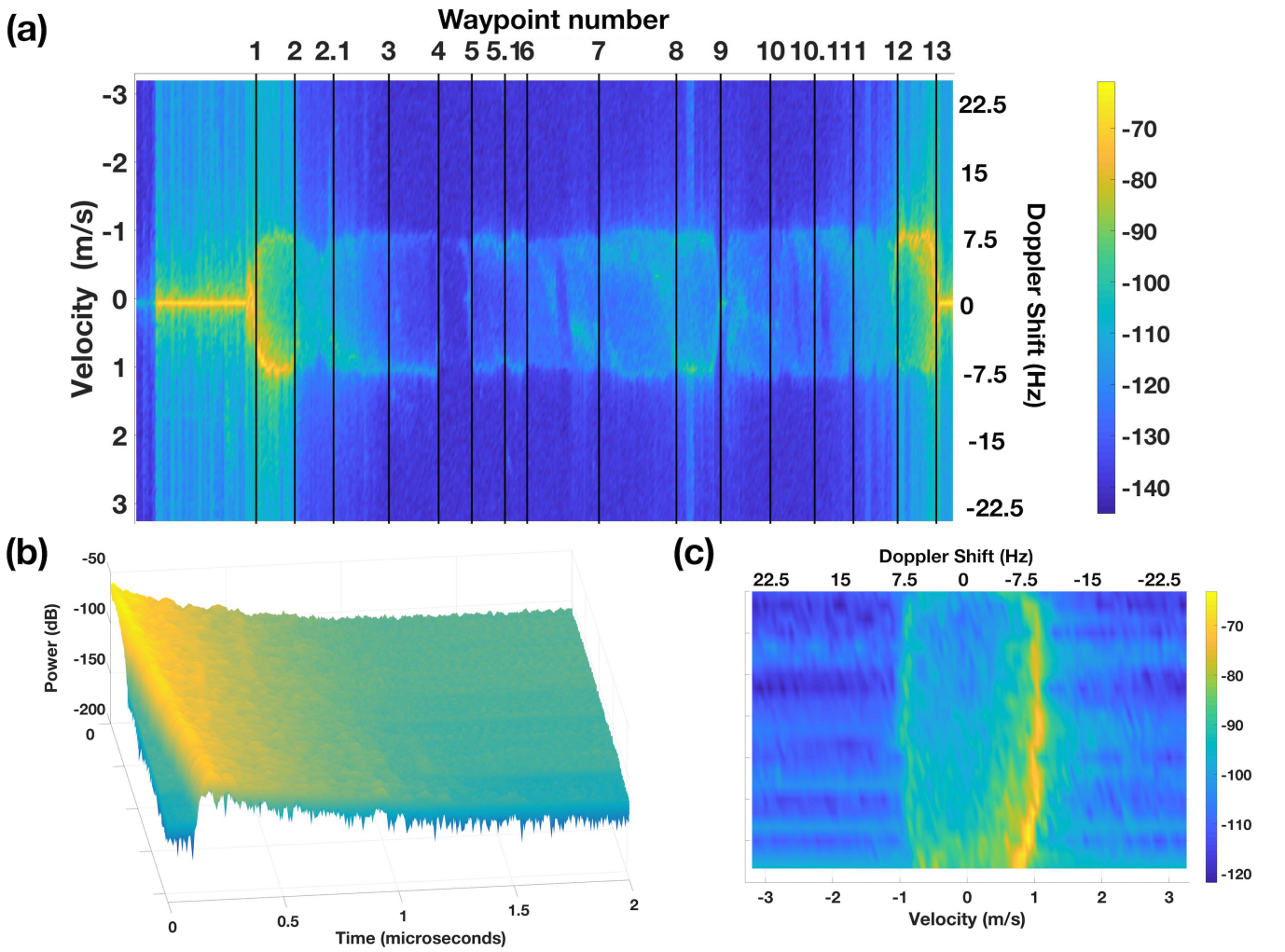

Fig. 7: (a) Velocity distribution over the long path with 2-s time resolution. (b) The slow fading of the PDP as the cart traveled from waypoint 1 to waypoint 2. (c) The velocity distribution for the same data shown in (b).

spectrum. The velocity of the peak power sample time gives the velocity of the receiver for this 6-second window. The fact that the primary peak is at roughly 1 m/s shows that manually pushing the cart was more accurate than we might expect.

We performed the same analysis for a short run, as shown in Figure 8(a), including where we paused with the cart for two 2-minute intervals at waypoints I3 and I6.1 in Figure 3(b). During this time, elevated equipment was moving at higher speeds around the receiver cart in the metal canyon. Figure 8(a) shows these two intervals as clear 0-velocity lines in the plot. To take a closer look at Doppler behavior in the metal canyon around location I3 and I6.1, Figure 8(b) and (c) give Doppler spectra (or velocity distribution) at region I3, in which the cart was stationary for 2 minutes, and along the path between I4 and I6.1, respectively. While there are features outside the 0-velocity peak in (b), we do not see any differences in this spectrum as we look at time bins spaced away from the maximum peak bin, t. This means that we are not seeing any strong fast fading effects from equipment moving near the receiver antenna. In Figure 8(c), the point of interest is that while the cart moves at roughly 1 m/s, the spectral region between +/- 1 m/s is also filled in. Note here that the cart is moving away from the transmit antenna, and in both (b) and (c), the equipment motion is confined to a gantry system running perpendicular to the line between transmitter and receiver cart.

To look at this further, Figure 9 shows the average Doppler spectra for panels 7(c), blue, and 8(c), red, as compared with the Doppler model for Rayleigh fading, yellow. At first order, Rayleigh fading applies to the case where scattering is from many surfaces, as is the case throughout our factory environment. Interestingly, although Rayleigh fading does not presuppose line-of-sight, our data from waypoint 1 to 2 for the outer run more closely resembles the Rayleigh model. The Doppler spectrum collected while walking in the metal canyon, combined with the earlier narrow observed rms delay spread (Figure 4(b)) suggest that propagation paths in this region are highly limited. These data also show limited power in the signal received for these regions.

The velocity analysis began with CIRs that were filtered using the PN filter and scaling factor discussed earlier. The PN filter, however, broadens the signal in time and lowers

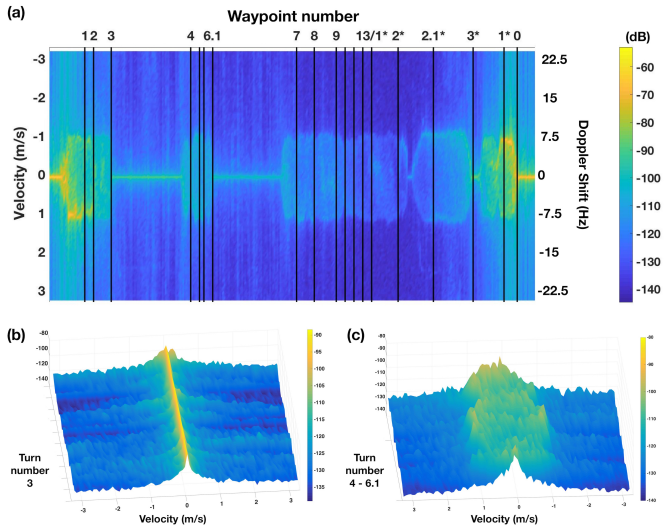

Fig. 8: (a) Velocity distribution over the short path with 2-s time resolution. In this short path, there are two dwell intervals of 2-minutes each shown by the prominent 0-velocity peaks. (b) The velocity distribution at the dwell period, waypoint I3. (c) The velocity distribution along the path in the metal canyon from waypoints I4 to I6.1.

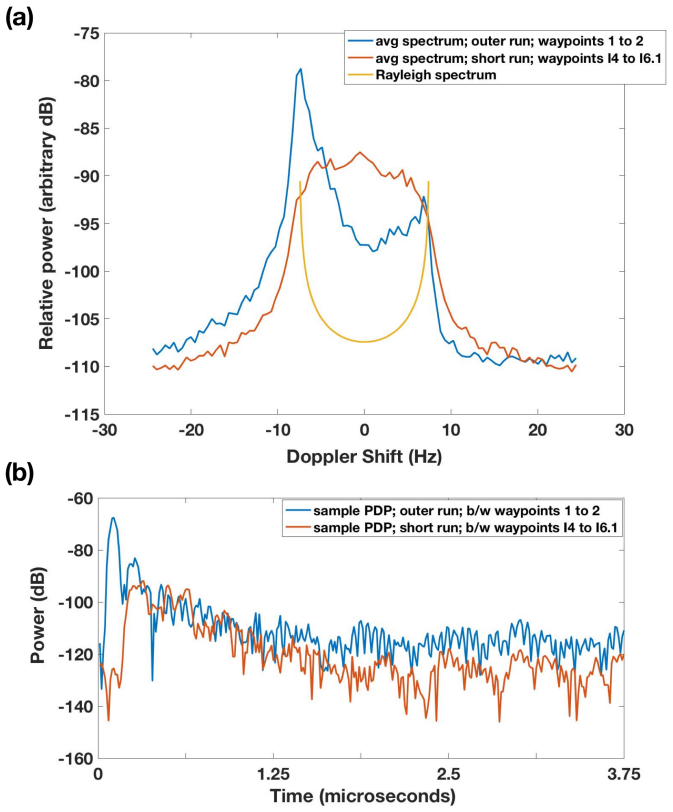

Fig. 9: Panel (a) compares the average Doppler spectrum from the region in Figure 7(c), blue curve, and Figure 8(c), red curve, and the Doppler model for Rayleigh fading, yellow curve. The y-axis is arbitrary because we have shifted the curves to have comparable noise floors. Panel (b) shows sample PDPs corresponding to the blue and red curves in panel (a).

the noise floor, running the risk of obscuring high velocity contributions. We performed the same analysis a second time using only the central 36 MHz of signal bandwidth across the entire run. While the noise floor is more prominent, no additional peaks appear other than those in the PN-filtered plot. This comparison eliminates the possibility that the PN filter has obscured the effect of fast-moving machinery passing by the receiver cart during the stationary period.

IV. Verification of Velocity

Up to this point, we have assumed that the cart velocity of 1 m/s is accurate. To verify the velocity results and assumed cart velocity from the factory environment, we followed up on this work with a further short-path measurement at 2.245 GHz in the front lobby of Building 1 at NIST Boulder Laboratories. A schematic of the setup is shown in Figure 10a. The primary driver for this measurement was to simultaneously collect laser tracker data and channel data. Using the same antennas and chassis setup, we collected data while walking a straight path roughly 60 ft from the transmit antenna, returning along the same route. We sampled at 200 MHz instead of 80 MHz, giving a 5-ns symbol rate. The PN codeword, arrangement of records and acquisitions, and PN filtering to generate CIRs were all kept the same. The laser tracker was set up at one end of the long lobby, near the transmit antenna. A spherical mirror reflector (SMR) was mounted on the receiver cart so that it was in the region of sight of the laser tracker for the entire run. As the operator pulled the cart away for the transmitter, both channel data collection and laser tracker data collection were initiated. At the end of the lobby, the operator stopped and returned to the transmit location. The laser tracker recorded the SMR position at a rate of 3 Hz, although timestamps only recorded to a precision of 1 second. CIR from this data were calculated as before in Equation 12, and the Doppler shifts and resulting velocity distribution followed from Equation 19. The cart velocity was then calculated from the laser tracker data such that:

$$v_n = \frac{\text{position}(n+1) - \text{position}(n)}{0.333\text{s}}, \tag{20}$$

where the collection of $(n+1)$ laser tracker data points would result in n points with known cart velocity. Figure 10b shows the laser tracker velocity and the Doppler-dervice velocity. Rather than displaying an entire velocity distribution for a particular time bin, as we did for the factory space, we only show the velocity of the dominant peak in the distribution. In the absence of other moving objects, this clearly shows the velocity of the cart moving away from and towards the transmit location. The velocity resolution of our laser tracker data was much higher than that of our channel data. We aligned the two data sets using the acquisition number turn at the north end of the run. The buffer time between acquisitions in the Doppler data was estimated at 1 s to give agreement in the start, turn, and stop times of the run relative to the laser tracker data. Since the run was short, with only one turn, this provides a more useful comparison than the turn identification used in the factory runs.

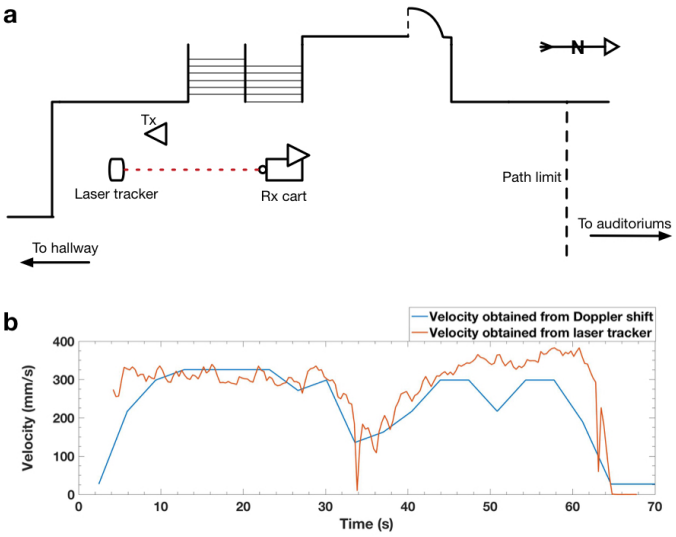

Fig. 10: (a) An approximate schematic of the experimental setup of data collection in the lobby of Building 1. The dash line marking the path limit both marks the place at which the lobby ceiling gets lower and the place at which we get out of range of the laser tracker. The red dashed line represents the line of sight between the laser tracker and the SMR. (b) Comparison of the velocity determined from the laser tracker data and from the Doppler-derived calculations.

Within the straight sections of the path, agreement between the Doppler-derived velocity and that measured by the laser tracker is generally good. Interestingly, the return path of the cart seems to show more of a cosine-like behavior in the velocity discrepancy between the laser tracker and the Doppler-calculated velocity. The transmitting antenna was 3.10 m in the air, and the farthest distance the cart reached was 18.3-m away. Since the distance along the floor is shorter than the path to the transmitter, it is reasonable that this behavior might appear as the cart approached. The other possibility is that the 300-record-long time period over which we calculate each velocity data point means that there is some averaging occurring, leading to less accurate velocities in regions of acceleration. Sampling the velocity in smaller bins (i.e. 100-record bins) would have decreased our velocity resolution while improving our spatial resolution. In the factory space, longer straight paths between turns, and the different sampling rate actually provided improved resolution (21.74 mm/s vs 54.35 mm/s) and more detailed path resolution. The claim that the velocity distribution data calculated from the factory space data accurately reflects the velocity of the cart holds true.

V. Conclusions

We have performed channel sounding measurements at 2.245 GHz and 5.400 GHz in an industrial space. The path walked through the factory environment produces slow fading behavior as evidenced in the time domain power delay profiles and time of first arrival. In order to see fast fading in this channel, the time-resolution of our sampling would have to be shorter than the coherence time of the signal. One way to accomplish this would have been to move the cart much faster, but given the safety constraints of the space, this was not feasible. Of importance, is the fact that industrial equipment that moved quickly overhead, such as the gantry systems in the metal canyon were also not observed to cause fading behavior, either because of their speed, or because their path was perpendicular to our line of sight in most instances. Other moving bodies in the factory space, such as automatically-guided vehicles, small motor electric vehicles, and heavy equipment, moved much more slowly, at speeds more comparable to our cart. A deeper study of the Doppler spectrum lies within the scope of future work, where an average spectrum, encompassing an entire path or path segment might be considered for each of the 8188 time bins. The chief factor, then, in the spread and fading of our received signals, was the large multi-path contribution from transmitting in such a dense and reflective environment and line-of-sight factors that contributed to overall received power. Velocity distributions calculated from impulse responses show the motion of the receiver cart to be the primary and possibly only contributor to slow fading of the signal. While different sampling times or signal bandwidth may have enabled our data collection to tell us more about the factory environment, the data present here show that for the deployment of wireless signals near the 2 and 5.4 GHz bands, fast or Doppler fading may not affect signal quality.

Acknowledgements

We would like to acknowledge work done in initial system setup by Luis Gonzales and post-processing work performed by Joe Diener at NIST Boulder Laboratories.

References

[1] D. R. Novotny, A. E. Curtin, J. T. Quimby, K. A. Remley, P. B. Papazian, and R. Candell, "A tetherless, aboslute-time channel sounder; processing and results for a complex environment," in *38th Annual Symposium of the Antenna Measurements Techniques Association*, (Austin, TX), 2016.

[2] J. T. Quimby, R. Candell, K. A. Remley, D. Novotny, J. Diener, P. B. Papazian, A. Curtin, and G. Koepke, "NIST channel sounder overview: Wireless platforms for smart manufacturing," *NIST Tech. Note XXXX*, 2016.

[3] P. B. Papazian, J.-K. Choi, J. Senic, P. J. Jeavons, C. A. Gentile, N. Golmie, R. Sun, D. R. Novotny, and K. A. Remley, "Calibration of millimeter-wave channel sounders for super-resolution multipath component extraction," *Proceedings of EuCAP 2016*, pp. 1–5, 2016.

[4] R. Candell, K. A. Remley, J. T. Quimby, D. Novotny, A. Curtin, P. B. Papazian, M. Kashef, and J. Diener, "Industrial wireless systems radio propagation measurements," *NIST Tech. Note 1951*, 2016.

[5] International Telecommunication Union Radiocommunication Sector, "Recommendation ITU-R P.1407-5: Multipath propogation and parameterization of its characteristics," 2013.

[6] A. H. Kemp and S. K. Barton, "The impact of delay spread on irreducible errors for wideband channels on industrial sites," *Wireless Personal Communications*, vol. 34, pp. 307–319, 2005.

[7] P. B. Papazian, C. Gentile, K. A. Remley, J. Senic, and N. Golmie, "A radio channel sounder for mobile millimeter-wave communications: System implementation and measurement assessment," *IEEE Transactions on Microwave Theory and Techniques*, vol. 64, 2016.